Preparation and study of Z-type heterojunction composite photocatalytic material with Ag$_2$MoO$_4$-modified rosette-like Bi$_2$WO$_6$ with Ag-SPR-promoting effect

Yufen Gu[1,2,*] and Bobo Guo[1]

[1] State Key Laboratory of Advanced Processing and Reuse of Nonferrous Metals, Lanzhou University of Technology, Lanzhou 730050, China

[2] Key Laboratory of Nonferrous Metal Alloy and Processing, Ministry of Education, Lanzhou University of Technology, Lanzhou 730050, China

ABSTRACT

Here, the novel Ag$_2$MoO$_4$/Bi$_2$WO$_6$ (AMO/BWO) heterojunction composite photocatalysts were synthesized based on the combination (co-precipitation method+hydrothermal method) XRD, XPS, SEM, TEM, UV–Vis DR spectroscopy, PL spectroscopy, FTIR spectroscopy, as well as EIS analyses were employed to characterize the photocatalysts, and photocurrent response was utilized to confirm the formation of Z-type heterojunction. The generation and transfer of electron/holes in the AMO/BWO heterojunctions excited by simulated sunlight were analyzed. Under simulated sunlight, the photocatalytic performance of AMO/BWO composites were studied by degradation of organic pollutants. The experimental results show that the 30 wt% AMO@BWO is the best photocatalytic composite material among all samples and the degradation rate reached 98.6%. Due to the prolonging of lifetime of the photoexcited electrons in the CB of AMO and holes in the VB of BWO, these carriers are more effective to participate in photodegradation reactions. An electron/hole transfer mechanism of the Z-scheme heterojunctions is proposed to illustrate the enhanced photodegradation performance of the AMO/BWO composite samples.

Address correspondence to E-mail: guyf@lut.cn

Springer

1 Introduction

Nowadays, along with the progress of society and rise of new industries, the chemical and pharmaceutical industries are developing rapidly; simultaneously various organic pollutants and chemical dyes are discharged into the environment, such as rhodamine B (RhB), methyl orange (MO), methylene blue (MB), tetrabromobisphenol A (TBBPA), and tetracycline hydrochloride (TC). Most of the organic pollutants are toxic, carcinogenic, chemically extremely stable, and they cannot self-decompose in most cases under natural conditions [1]; thus, the green and environment-friendly methods to manually remove these hazardous organic pollutants are desired. In recent years, semiconductor-based photocatalysis technology has developed rapidly, which is a new and green technology, and has been widely used in organic pollutant degradation, sterilization, and water separation [2, 3]. Compared with traditional treatment methods of organic pollutants, including physical adsorption [4], chemical reaction [5] and biodegradation [6], photocatalysis technology is advanced, non-toxic, convenient and simple operation, no secondary pollution to the environment and lower cost [7], so it is necessary for us to design and construct Z-type, p-n type and other heterojunctions composite semiconductor photocatalytic materials with visible light response [8]. Construction of heterojunction can not only inhibit the recombination of photogenerated electrons and holes, but also broaden the absorption range of the spectrum [9]. In the photocatalysis process, the main active species are hydroxyl radicals, superoxide radicals, and holes, which are the most important factors for the catalytic oxidation of organic pollutants [10, 11].

Silver-based semiconductors have been a hot topic in recent years due to their excellent photocatalytic efficiency. Moreover, the element silver has surface plasmon resonance, which will broaden the spectral response and further play the role in transferring photogenerated electron/hole. Among them, Ag_2MoO_4 (AMO) has a relatively low VB and CB position, suggesting that AMO can be combined with most other photocatalytic materials to build heterojunctions with special photocatalytic performances [12, 13]. The nature and the strong potential to generate hydroxyl radicals and good electrical conductivity have attracted strong attention [14–16]. However, AMO is a wide band gap n-type semiconductor, which can only be excited under ultraviolet light ($\lambda < 380$ nm) [17]. The low-light absorption range and poor photocatalytic performance lead to its rare application in the field of photocatalysis [18]. As we all know, the surface silver ions of most silver-based photocatalytic materials will be reduced to metallic silver due to light corrosion under the sunlight, so as AMO [19, 20].

Bismuth tungstate (Bi_2WO_6, BWO) is also one of the most popular semiconductors in recent years. The Aurigillius-type BWO has a special crystal structure, which is a layered structure and has a suitable light absorption range. In addition, it also has a W 5d orbital guide conduction band (CB), and special valence band (VB) formed by O 2p and Bi 6 s hybrid orbitals. The special layered structure and energy band structure endow BWO excellent photocatalytic performance [21] for wastewater treatment and photoreduction to prepare CO_2. However, in the process of photocatalytic degradation of pollutants, there is also a fast and easy recombination of photogenerated electron/hole, which greatly limits its photocatalytic performance. Different heterojunctions have been built through the load of precious metals (such as silver and silver nanowires, gold, platinum nanoparticles) and other semiconductors. For example, MoS_2/Bi_2WO_6, Ag_3VO_4/Bi_2WO_6, $g\text{-}C_3N_4/Bi_2WO_6$, $Bi_2WO_6/BiOI$, and Fe_3O_4/Bi_2WO_6 have exactly confirmed that the construction of heterojunctions can improve the photocatalytic performance [22–26].

In this work, we adopted a combine method—hydrothermal method+co-precipitation method—to self-assemble AMO particles onto BWO. The constructed AMO/BWO heterojunction photocatalysts have excellent performance for the separation and transfer of photogenerated holes and electrons. The photocatalytic performance of as-prepared AMO@BWO photocatalytic materials was investigated under simulated sunlight. The optimal composite sample is confirmed to be 30 wt% AMO@BWO according to the photodegradation of RhB. Further, we have studied the application of the 30 wt% AMO@BWO composite material in photocatalytically degrading other typical organic dyes and pollutants.

2 Experimental

2.1 Materials

All reagents used are of analytical grade and no further processing is required: $Bi(NO_3)_3 \cdot 5H_2O$, purchased from Shanghai Aladdin Biochemical Technology Co., Ltd., $Na_2WO_4 \cdot 2H_2O$, purchased from Tianjin Damao Chemical Reagent Factory, CH_3COOH, purchased from Guangdong Guanghua Technology Co., Ltd., CH_3CH_2OH, purchased from Guangzhou City Jinhua University Chemical Reagent Co., Ltd., $Na_2MoO_4 \cdot 2H_2O$, $AgNO_3$ is West Asia reagent, and Shandong West Asia Chemical Industry Co., Ltd.

2.2 Preparation of rosette-shaped BWO

The rosette-like BWO was prepared by a hydrothermal method. First, 0.9702 g (0.002 mol) Bi $(NO_3)_3 \cdot 5$-H_2O were dissolved it in 20 mL of glacial acetic acid, and stirred it magnetically for 30 min until there were no suspended particles, as solution A. Then 0.3298 g (0.001 mol) $Na_2WO_4 \cdot 2H_2O$ were dissolved it in 20 mL of deionized water, stirred it magnetically for 30 min as solution B. The solution B was slowly added dropwise to the solution A for 30 min. deionized water (30 mL) was added to above mixture solution, and then transferred to a 100 mL polytetrafluoroethylene liner. The liner was put into the autoclave to seal; The hydrothermal reaction was carried out at 200 °C for 24 h. Finally, the precipitate were collected, washed and dried to obtained the BWO sample.

2.3 Preparation of AMO@BWO composite catalyst

In a typical composite sample preparation process, 0.4 g of the prepared BWO were dispersed in 40 mL of deionized water, which was stirred magnetically for 30 min. 0.1549 g of $AgNO_3$ were dissolved in the above solution, and then magnetically stirred for 60 min as solution C. 0.1103 g of $Na_2MoO_4 \cdot 2H_2O$ were dissolved in 20 mL of deionized water with magnetically stirring for 30 min as solution D. The solution D was slowly added to the solution C and stirred magnetically for 4 h. The whole process was carried out under shading. Finally, the precipitate were collected, washed and dried to obtained 30 wt% AMO@BWO composite sample. 20 wt% AMO/BWO and 40 wt% AMO/BWO composites were also prepared with different AMO mass percentages using the same sample preparation route. The schematic preparation process of the 30 wt% AMO@BWO composite sample is shown in Fig. 1.

2.4 Sample characterization

D8 advanced X-ray diffractometer to was used to obtain the XRD pattern of the samples to analyze the crystal structure ($\lambda_{Cu-k\alpha} = 0.15406$ nm, 10° to 90° as the 2θ scanning range). UV–Vis DRS spectra were measured using TU-1901 dual beam spectrophotometer. XPS measurement was carried out on PHI-5702 multifunctional X-ray photoelectron spectrometer. The transmission electron microscope and scanning electron microscope analysis of the sample were, respectively, used JEM-1200EX field emission transmission electron microscope and JSM-6701F field emission scanning electron microscope. Dual-spectrum infrared spectrophotometer was used to measure FIR spectra. Radio frequency RF-6000 fluorescence spectrophotometer was used to measure fluorescence spectrum (excitation wavelength 270 nm). The electrochemical impedance spectroscopy (EIS) and photocurrent response were measured on the CST 350 electrochemical workstation. The working electrode preparation procedure was described in the previous publication [27]. Simulated sunlight emitted by a 300-W xenon lamp (PLS-SXE300 BF) with a light power of 50 W was use as the light source. The parameters and measurement process were described in the literature detailedly [27].

2.5 Photodegradation performance testing

In this study, the organic pollutants MB aqueous solution ($C_{MB} = 5$ mg L^{-1}), MO aqueous solution ($C_{MO} = 5$ mg L^{-1}), RhB aqueous solution ($C_{RhB} = 5$ mg L^{-1}), MB/MO/RhB mixed aqueous solution ($C_{MB} = C_{MO} = C_{RhB} = 5$ mg L^{-1}), TC aqueous solution ($C_{TC} = 5$ mg L^{-1}), TBBPA aqueous solution ($C_{TBBPA} = 5$ mg L^{-1}) were used to analyze the photocatalytic performances of the samples. 100 mL of pollutant solution and 0.03 g of catalyst were used as the photoreaction solution. Before using a 300-W xenon lamp (PLS-SXE300 BF solar simulator) to irradiate the reaction solution to initiate photocatalysis, the photocatalyst and the photoreaction solution were adsorbed for 30 min in a dark environment. Then, a certain
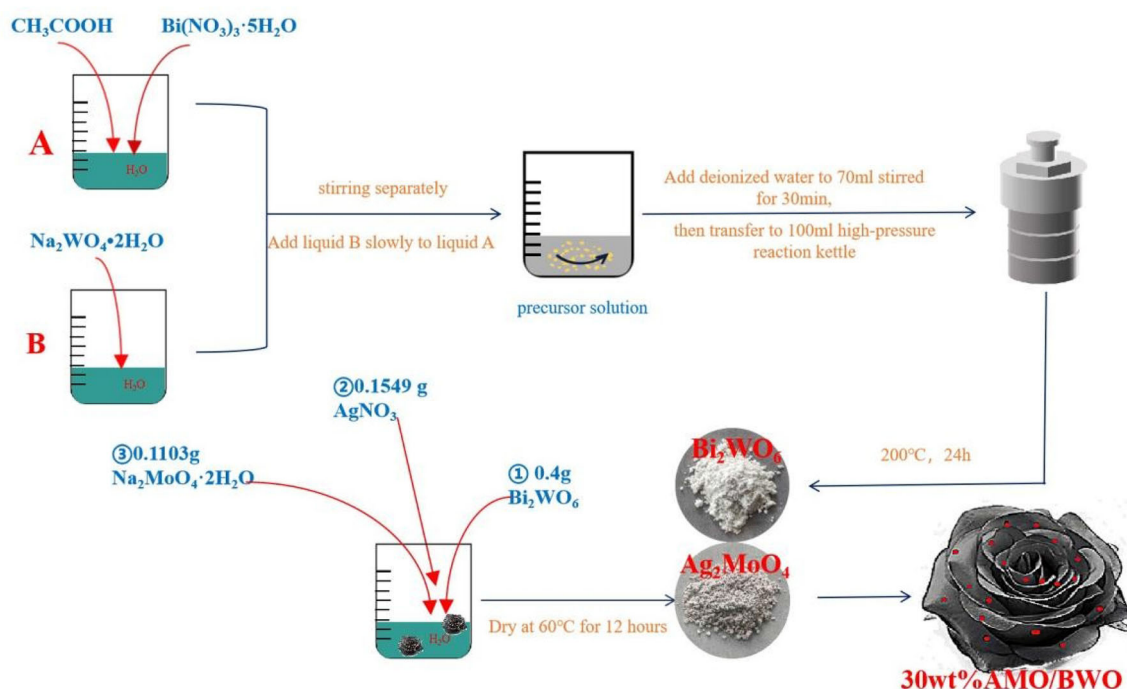
Fig. 1 Schematic preparation process of 30 wt% AMO/BWO composite

reaction was pipetted out and put into a 5 mL centrifuge tube, and centrifuged to remove the photocatalyst in the reaction solution in the process of photocatalytic degradation of pollutants. UV–Vis absorption spectra of the reaction solution were measured on an UV759 UV–Vis spectrophotometer. According to the absorbance change at the maximum absorption wavelength, the residual concentration of the pollutant was obtained. Using the formula $\eta = (1 - C_t/C_0) \times 100\%$ ($C_0 \rightarrow$ initial pollutant concentration, $C_t \rightarrow$ residual pollutant concentration at t min) to calculate the degradation efficiency (η).

3 Results and discussion

Figure 2 shows the XRD patterns of as-prepared 30 wt% AMO@BWO, AMO, and BWO. It can be seen that the BWO spectrum is completely matched with the standard diffraction card PDF#73–2020, and there was no impurity peak, which indicates that the BWO prepared by the experiment is the pure orthorhombic crystal structure with the unit cell parameter a = 0.5457 nm, b = 0.5436 nm and c = 1.6427 nm. In addition, all the diffraction peaks of AMO are in good agreement with the standard diffraction card PDF#08–0473 [20, 28], and no other irrelevant
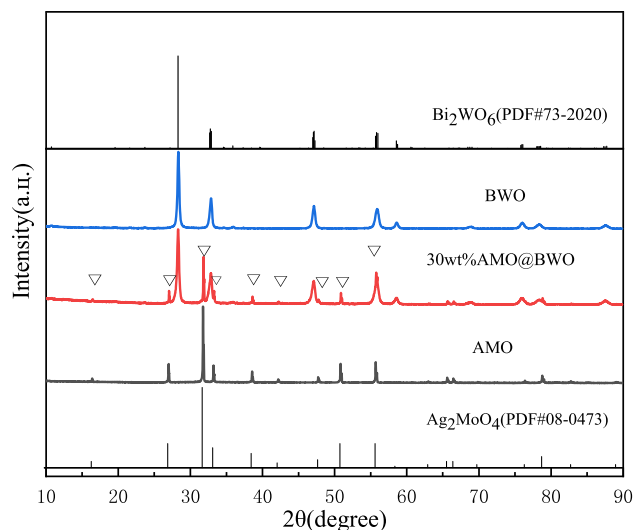
Fig. 2 XRD patterns of AMO, BWO and 30 wt% AMO/BWO

diffraction peaks are found. This implies the synthesis of pure cubic AMO with the unit cell parameter a = b = c = 0.9313 nm. Moreover, the diffraction peak of AMO was very narrow, indicated that the grain size of AMO is large. For the 30 wt% AMO@BWO composite material, obviously AMO diffraction peaks can be observed, where $2\theta = 2.05$, 31.82, 33.29, 38.62, 42.19 and 47.78 correspond to the crystal planes (220), (311), (222), (400), (331) and (422), indicating that

AMO and BWO co-exist in the AMO@BWO composite. The crystal structure of AMO and BWO do not change. In addition, all the diffraction peak positions of the 30 wt% AMO@BWO composite material agree with the diffraction peaks of bared AMO and BWO without other impurity diffraction peaks, indicating that the AMO@BWO composite photocatalyst has been successfully prepared.

Figure 3a shows the UV–Vis DRS spectra of AMO, BWO, and AMO@BWO composite materials. The band gap and optical absorption properties of the samples are analyzed using ultraviolet–visible diffuse reflectance spectroscopy. The photocatalytic performance of a photocatalytic material is closely related to its absorption of light. It is clear that the bare BWO sample has a remarkable light absorption in the wavelength range below 400 nm. Whereas the bare AMO has obvious light absorption in the wavelength range above 400 nm, which is significantly stronger than BWO. When AMO nanoparticles are deposited on BWO, the derived AMO@BWO composite sample have much higher strong visible light absorption than bare BWO, indicating a synergistic effect between the two semiconductors. In addition, the degree of absorption of visible light by the samples can be also judged from their colors. The color of the 30 wt% AMO@BWO composite sample is obviously darker than that of the bare BWO and

AMO. It can be seen from Fig. 3c–e that bare BWO and AMO have milky white and reddish colors, respectively. In contrast, the 30 wt% AMO@BWO composite sample exhibits a grayer color than that of bared AMO and BWO. The differential curves of the ultraviolet–visible DR spectra are used to estimate the band gap of the samples [29]. As shown in Fig. 3b, the absorption edges of AMO and BWO are 363.4 and 419.5 nm, respectively, indicating that the band gap of AMO is 3.41 eV, and the band gap of BWO is 2.96 eV, whereas the band gap of the AMO@BWO composite sample does not change significantly.

By measuring the FTIR spectroscopy of the as-prepared samples (Fig. 4), the possible presence of functional groups on their surface can be further diagnosed. The Fourier transform infrared spectrum of AMO shows obvious Mo–O tensile vibration at 830 cm^{-1}, which belongs to the characteristic stretching vibration signal of cubic structure AMO [30]. In the Fourier transform infrared spectrum of BWO, one can detect Bi-O stretching vibration (830 cm^{-1}), W–O stretching vibration (580 cm^{-1}) and W–O-W bridge stretching vibration (732 cm^{-1}), which are the characteristic absorption peaks of the well-known BWO with orthogonal structure [31, 32]. For the infrared spectrum of the 30 wt% AMO@BWO composite sample, there are both the characteristic absorption peaks of BWO and AMO, indicating that
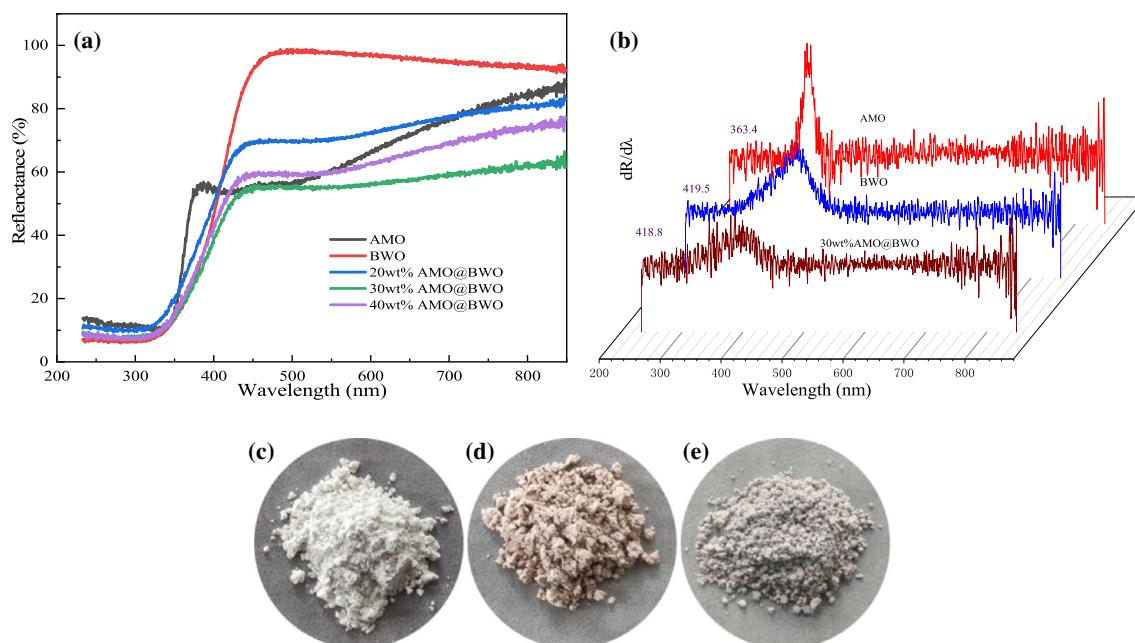
Fig. 3 a Ultraviolet–visible DR spectra of BWO, AMO and AMO/BWO composite materials; b Differential curves of the ultraviolet–visible DR spectra; c-e apparent colors of BWO, AMO and 30 wt% AMO/BWO, respectively
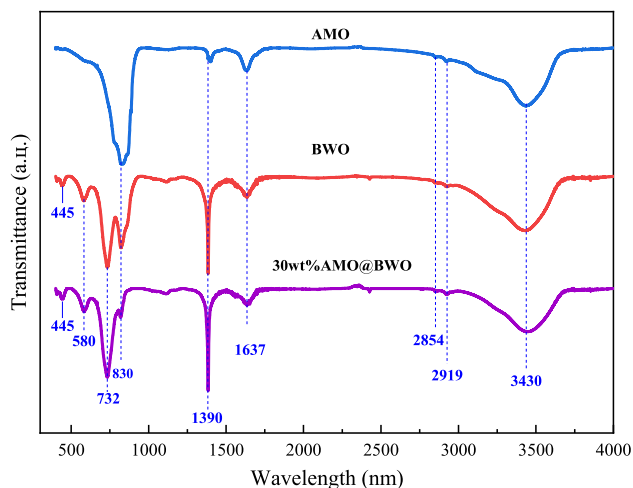
Fig. 4 FTIR spectra of AMO, BWO and 30 wt% AMO/BWO

AMO and BWO can be well coupled. For all samples, the characteristic absorption peaks detected at 1390, 2854 and 2919 cm^{-1} belong to the antisymmetric stretching vibration of the CO_3^{2-} group, while the absorption peaks at 1637 and 3430 cm^{-1} are attributed to the hydrogen–oxygen bending vibration and hydrogen–oxygen, respectively. The absorption peaks prove that there are CO_3^{2-} groups and H_2O molecules attached to the surface of the samples [33, 34].

Figure 5 shows the XPS spectra tested on the 30 wt % AMO@BWO composite sample. The C element in the full spectrum is used as a reference for the binding energy scale. Figure 5a is a full scan XPS spectrum, which clearly shows that the composite sample contains five chemical elements, namely Bi, W, O, Mo, and Ag. From the Bi-4f XPS spectrum (Fig. 5b), it can be seen that the binding energy positions of Bi-4f$_{7/2}$ (159.2 eV) and Bi-4f$_{5/2}$ (164.5 eV) indicate that the Bi species exists in the Bi^{3+} oxidation state [31, 35]. From the W-4f core-level XPS spectrum (Fig. 5c), it can be seen from the binding energy positions of W-4f$_{7/2}$ (35.4 eV) and W-4f$_{5/2}$ (37.5 eV) suggest that W^{6+} species exist in the BWO crystal [31]. Two characteristic peaks of 530.2 and 531.7 eV are detected on the O-1 s core level XPS spectrum (Fig. 5d), which correspond to lattice oxygen and chemisorption oxygen, respectively [29, 35]. The XPS spectrum of Mo-3d core energy level (Fig. 5e) shows two peaks at 231.8 and 235.0 eV, which coincide with the binding energy of Mo^{6+}-3d$_{5/2}$ and Mo^{6+}-3d$_{3/2}$, respectively [36]. Figure 5f is the Ag-3d core-level XPS spectrum. The two main peaks of 367.4 (Ag^{+}-

3d$_{5/2}$) and 373.4 eV (Ag^{+}-3d$_{3/2}$) match with the lattice Ag^{+} of AMO. The two weak peaks at 368.3 (Ag^{0}-3d$_{5/2}$) and 374.3 eV (Ag^{0}-3d$_{3/2}$) correspond to the metallic silver species [37] generated during the preparation of composite samples.

SEM images were measured to analyze the morphology of BWO, AMO and 30 wt% AMO@BWO. As seen from Fig. 6a, AMO exists in the form of ellipsoidal or spherical particles in the range of 1.8 to 3.8 μm. The SEM image of BWO (Fig. 6a) shows that the BWO crystals are self-assembled into rosette-like hierarchical structure with size of 3–9 μm. The hierarchical structure is assembled from nanosheets with a diameter of 300–2200 nm and a thickness of 20–40 nm. For 30 wt% AMO@BWO composite sample, the AMO particles are self-assembled on the petals of the BWO rosette flower, and the particle size of the AMO is reduced to 30 to 70 nm. The reason for this phenomenon may be that the silver ions are pre-adsorbadon the petals of BWO, and the growth of AMO is greatly restricted [38]; furthermore, the hierarchical structure of BWO could affect the surface energy of AMO crystals and restrict their growth. The TEM image suggests a good contact between AMO with BWO, thus establishing a stable photo-generated hole and electron transfer path between them and promoting effective separation and transfer of carriers. In addition, the composite material compounded with rosette-like BWO has a larger specific surface area and provides more active sites for the photodegradation reactions of pollutants.

In contrast with SEM technique, TEM offers a bigger advantage in revealing the microstructures of functional materials [39]. The microstructure of 30 wt % AMO@BWO was further analyzed by TEM images to reveal the formation of heterojunctions established between AMO and BWO. It can be clearly seen from Fig. 6a and b that the AMO particles are well self-assembled and fixed on the petals of the rosette-like BWO. On the surface of the composite material, metal silver nanoparticles of smaller size can be also seen. This may be due to the reduction of a few silver ions into silver nanoparticles during the sample preparation process. High-resolution TEM (HR-TEM) image can further prove the formation of Ag/AMO/BWO heterojunctions, as shown in Fig. 7c. In the HR-TEM image, AMO and BWO crystals and Ag nanoparticles can be identified by the characteristics of their lattice fringes. Figure 7k shows the selected area electron diffraction (SAED) pattern, on which the
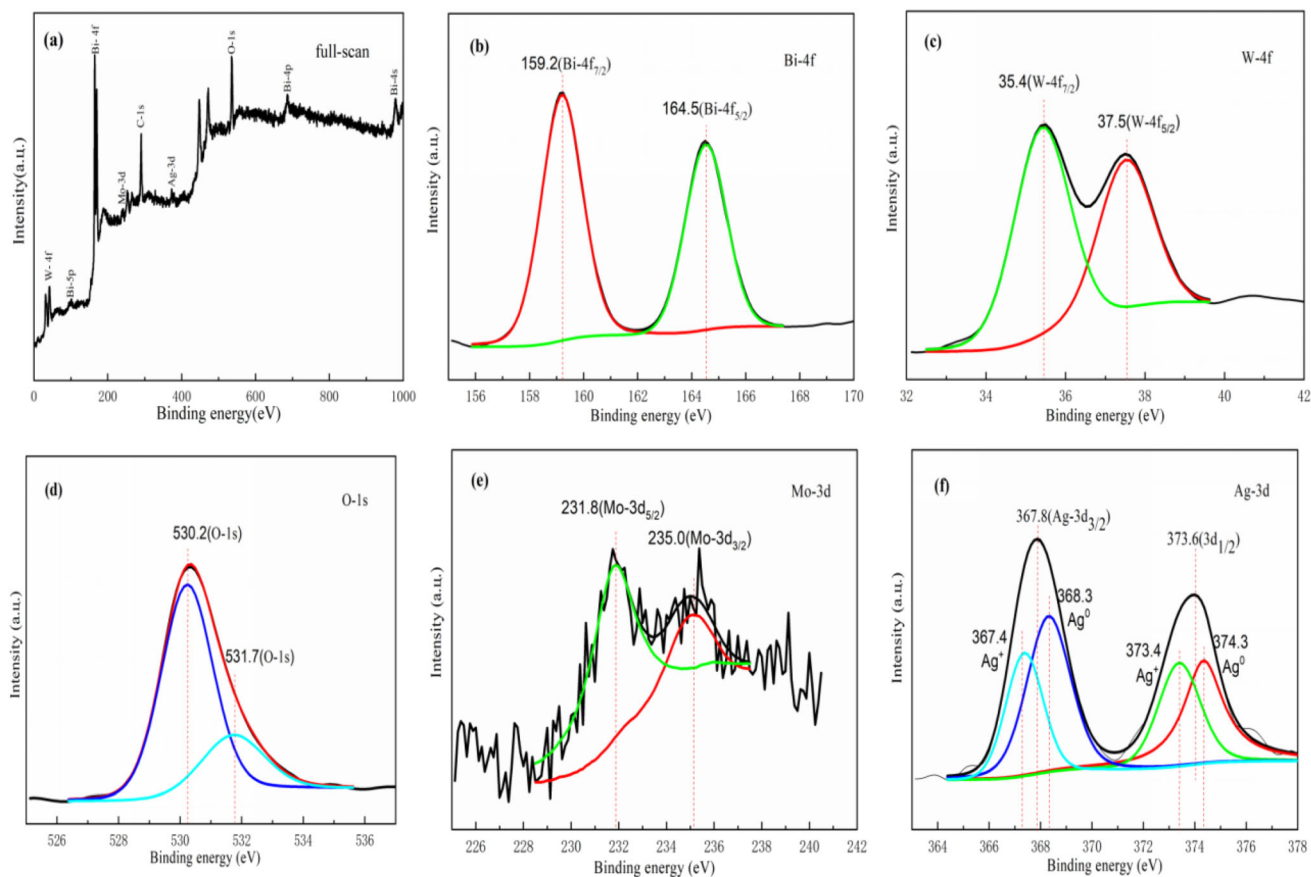
Fig. 5 **a** ful-scan, **b** Bi-4f, **c** W-4f, **d** O-1 s, **e** Mo-3d and **f** Ag-3d core level XPS spectra of 30 wt% AMO/BWO

polycrystalline diffraction rings clearly appear. Referring to the standard diffraction data of PDF#08-0473 (AMO cubic phase), PDF#73-2020 (BWO orthogonal phase) and PDF#87-0598 (Ag orthorhombic phase), polycrystalline diffraction rings can be well indicated. From the perspective of chemical elements, energy dispersive x-ray spectroscopy (EDS) can support the formation of heterojunctions between AMO and BWO, as shown in Fig. 7d. In addition to the Cu/C signals of the TEM micro-mesh support [40], the chemical elements Bi/W/Ag/Mo/O are also clearly detected on the EDS spectrum. The EDS element mapping images obtained from the dark field scanning TEM (DF-STEM) image area are shown in Fig. 7e–j. The elements are uniformly distributed on the composite material, indicating a uniform coupling between the AMO particles and the BWO layered architecture.

The recombination behavior of hole-electron pairs in semiconductors can be predicted by PL fluorescence spectra, photocurrent response spectra and EIS spectra. Figure 8 shows the fluorescence spectra of bare BWO and AMO@BWO composite samples (excitation wavelength: 270 nm). It is noted that when electron–hole pairs recombine, a certain fluorescence intensity will be produced. The stronger the fluorescence intensity of the sample is, the higher the recombination efficiency of electron–hole pairs [20]. In short, the stronger fluorescence intensity implies lower photocatalytic performance of the sample [41, 42]. It can be observed from the fluorescence spectra that the PL emission peaks of BWO and its derivative composite samples are between 400 nm and 450 nm [43]. However, the fluorescence intensity of the AMO@BWO composite samples is significantly lower than that of the bare BWO sample. The loaded AMO nanoparticles can effectively promote the separation and transfer of hole-electron pairs, which is conducive to improving the photocatalytic performance of the composite samples.

Figure 9a shows the photocurrent response spectra of AMO, BWO and 30 wt% AMO@BWO. Under simulated sunlight irradiation with a gap of 20 s (10 s of light and 10 s of darkness), all samples show
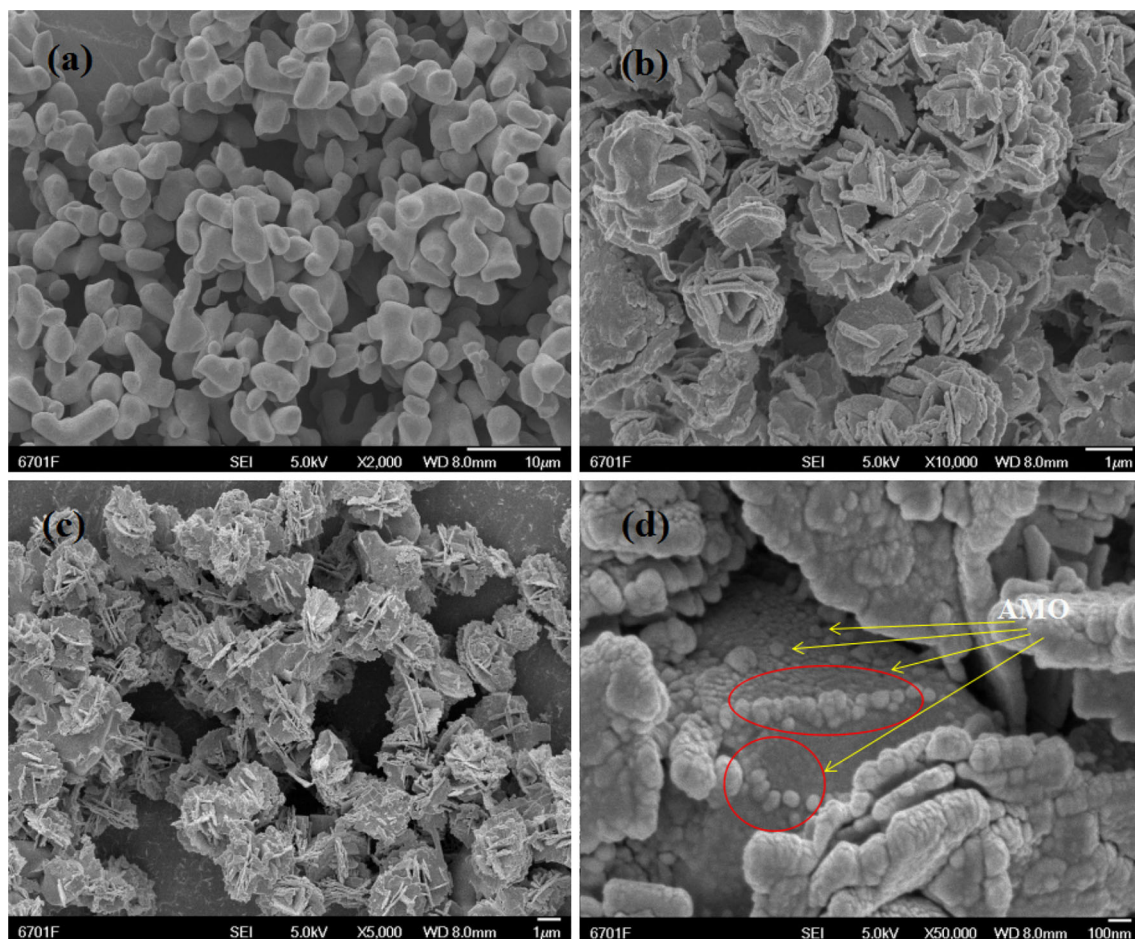
**Fig. 6** SEM images of **a** AMO, **b** BWO, and **c–d** 30 wt% AMO/BWO

obvious transient photocurrent response behavior. The order of photocurrent is AMO<BWO<30 wt% AMO/BWO.

Figure 9b depicts the EIS spectra (Nyquist format) of the samples. It can be seen that compared with bare BWO and AMO, the 30 wt% AMO/BWO composite has an EIS spectrum with a smaller semicircular diameter in the high frequency region. The semicircle diameter of the EIS is usually used as an indicator of the charge transfer resistance at the electrode/electrolyte interface [44]. The EIS spectrum shows that the charge transfer resistance of the 30 wt% AMO/BWO composite is small. PL spectra, photocurrent response spectra and EIS spectra can jointly indicate that the 30 wt% AMO/BWO composite sample exhibits a more effective separation and transfer of photogenerated electron–hole pairs compared with bare BWO.

The photocatalytic degradation performances of AMO, BWO, and AMO@BWO composites were compared by degrading RhB (C_{RhB}=5 mg L^{-1}, $C_{photocatalyst}$=0.3 g L^{-1}). Figure 10a–e display the UV–Visible absorption spectra of RhB solutions photodegraded by AMO, BWO, 20 wt% AMO@BWO, 30 wt% AMO@BWO, and 40 wt% AMO@BWO within 60 min, respectively. During the photodegradation process, the determination of the residual concentration of RhB is based on the absorbance of RhB at its maximum absorption wavelength ($\sim$ 554 nm). Figure 10f shows the photodegradation curves of RhB over different catalysts. It can be clearly seen that the photocatalytic performance of the AMO/BWO composites is much better than that of bare AMO and BWO. This specific phenomenon indicates that the heterojunctions are formed in the AMO/BWO composite materials, which is conducive to improving the separation efficiency of photogenerated electron–hole pairs, and synergistically enhancing the photocatalytic performance of the materials.
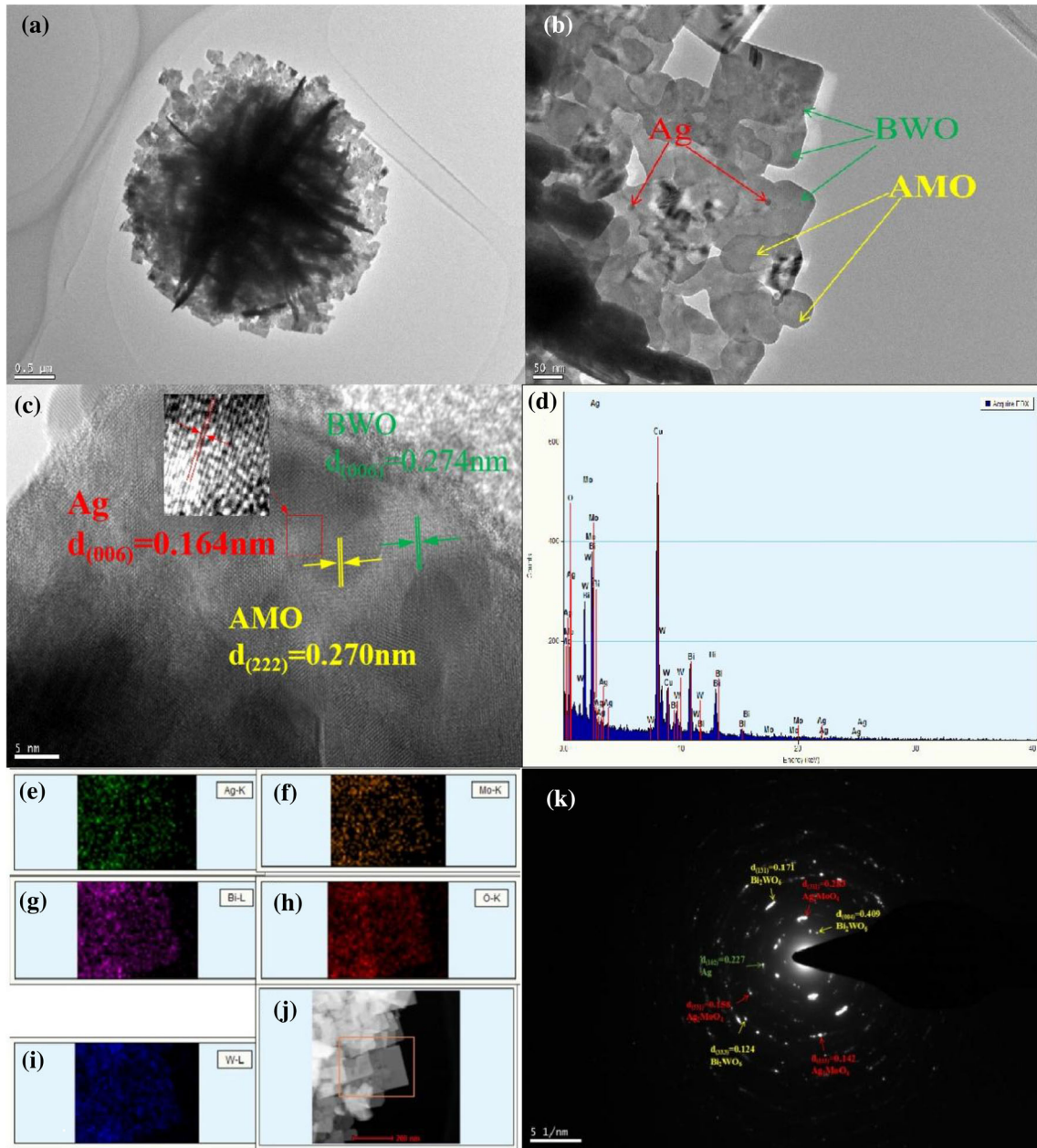
Fig. 7 TEM images (**a**, **b**), HR-TEM image (**c**), EDS spectrum (**d**), (**e-i**) EDS element mapping images and (**j**) DF-STEM image of 30 wt % AMO/BWO, SAED pattern (**k**)

Among the samples, the 30 wt% AMO/BWO composite shows the highest photocatalytic degradation performance. RhB is almost completely degraded within 60 min, and the degradation rate is as high as 98.6%, which is far higher than that of bared AMO (ŋ=29.5% within 60 min) and BWO (ŋ= 39.6% within 60 min). An important parameter to quantitatively compare the photodegradation performance of photocatalysts is the reaction rate constant [45]. Figure 10g depicts the Ln (C$_t$/C$_0$) ~ t
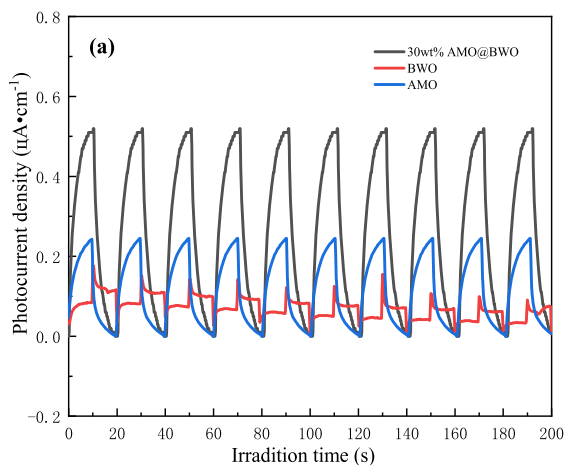
curves, from which it can be seen that the photodegradation process of RhB completely follows the pseudo first-order kinetics, expressed by Ln (C$_t$/C$_0$)= − k_{app}t [44, 46]. By comparing the apparent first-order reaction rate constants (k_{app}) between samples, the photodegradation performance of the best composite sample 30 wt% AMO/BWO (k_{app}=0.06186 min^{-1}) is estimated to be approximately 10.47 times higher than that of bare AMO (k_{app}=0.00591 min^{-1}) and 7.44
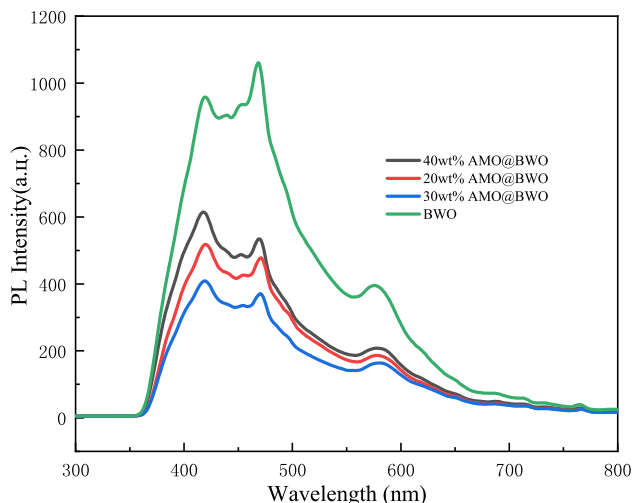
Fig. 8 Photoluminescence spectra of BWO and AMO@BWO composites measured at 270 nm excitation wavelength

Fig. 10 a–e UV–visible absorption spectra of AMO, BWO, 20 wt% AMO@BWO, 30 wt% AMO@BWO, 40 wt% AMO@BWO, respectively; **f** and **g** Photodegradation curves and pseudo-first-order kinetic diagrams of RhB degradation over the samples

times higher than that of bare BWO (k_{app}= 0.00831 min^{-1}).

To apply the most ideal 30 wt% AMO/BWO photocatalytic material to environmental purification in real life, we further evaluate its photodegradation performance by degrading MB, MO, RhB/MO/MB mixture, TC and TBBPA solutions. The concentration of MO, RhB and MB in the mixed solution can be estimated based on the absorbance at the maximum absorption wavelength of the dyes λ_{MO}=464 nm, λ_{RhB} =554 nm and λ_{MB}=663 nm. Figure 11a and b show the ultraviolet–visible absorption spectra of MB and MO, respectively. According to the ultraviolet–visible absorption spectra, the photodegradation curves of MB and MO can be obtained, as shown in Fig. 11c and d, respectively. It is seen that the degradation

rate of MB solution can reach 95.3% in 7.5 min, and the degradation rate of MO solution can reach 89.2% in 120 min. Under the action of the photocatalyst, MB and MO are basically removed.

Figure 11e and f display the UV–Vis absorption spectra of the RhB/MO/MB mixed solution (C_{MO}= C_{RhB}=C_{MB}=5 mg L^{-1}, $C_{photocatalyst}$=0.3 g L^{-1}) and the photodegradation curves of RhB, MO and MB. Interestingly, in the photodegradation progress of the mixed dyes, it can be found that MB and MO are degraded preferentially than RhB, and within 50 min, the degradation rates of MB and MO reach 95.5% and 80.4%, respectively. When the irradiation time exceeds 100 min, the C_t/C_0 ratios of MB and MO remain basically stable. In contrast, the photodegradation of RhB is relatively slow, basically meeting with the quasi-first-order kinetic process. Possibly the ionization of the dye, the molecular structure of the dye, the catalyst's promotion of the decomposition of the dye, the synergistic photosensitivity effect between different dyes and the adsorption characteristics of the catalyst to different dyes collectively result in the competitive photodegradation of dyes in the mixed solution.

Figure 12a and b show the UV–Vis absorption spectra of TC and TBBPA solutions photocatalyzed by 30 wt% AMO/BWO composite photocatalyst. The concentrations of TC and TBBPA are usually


Fig. 9 Photocurrent spectra (**a**) and EIS spectra (**b**) of AMO, BWO and 30 wt% AMO@BWO
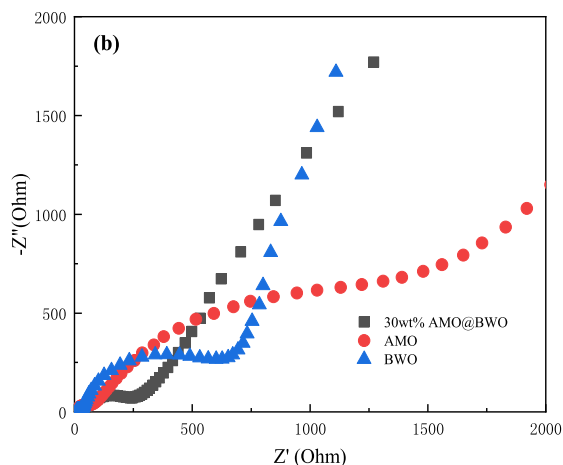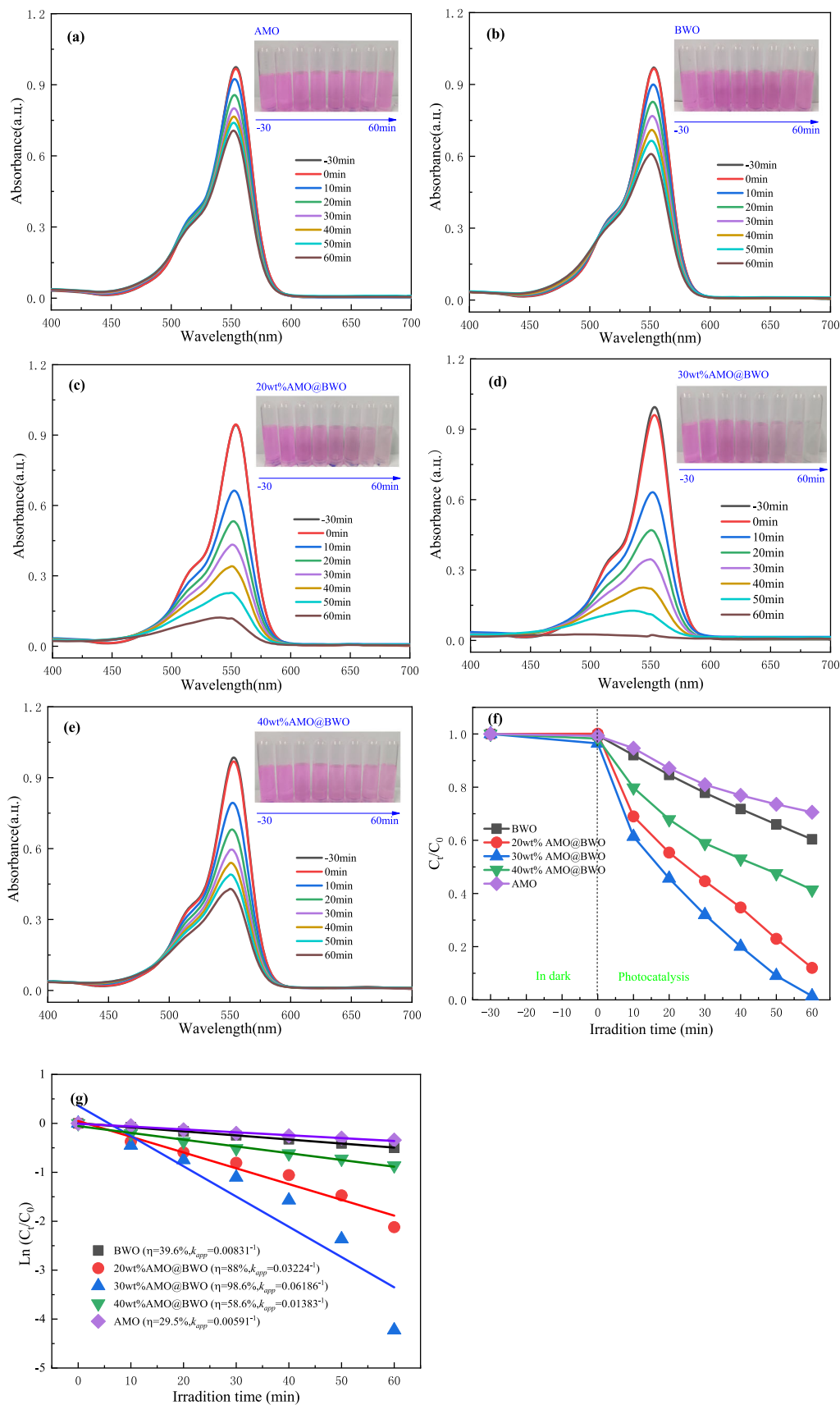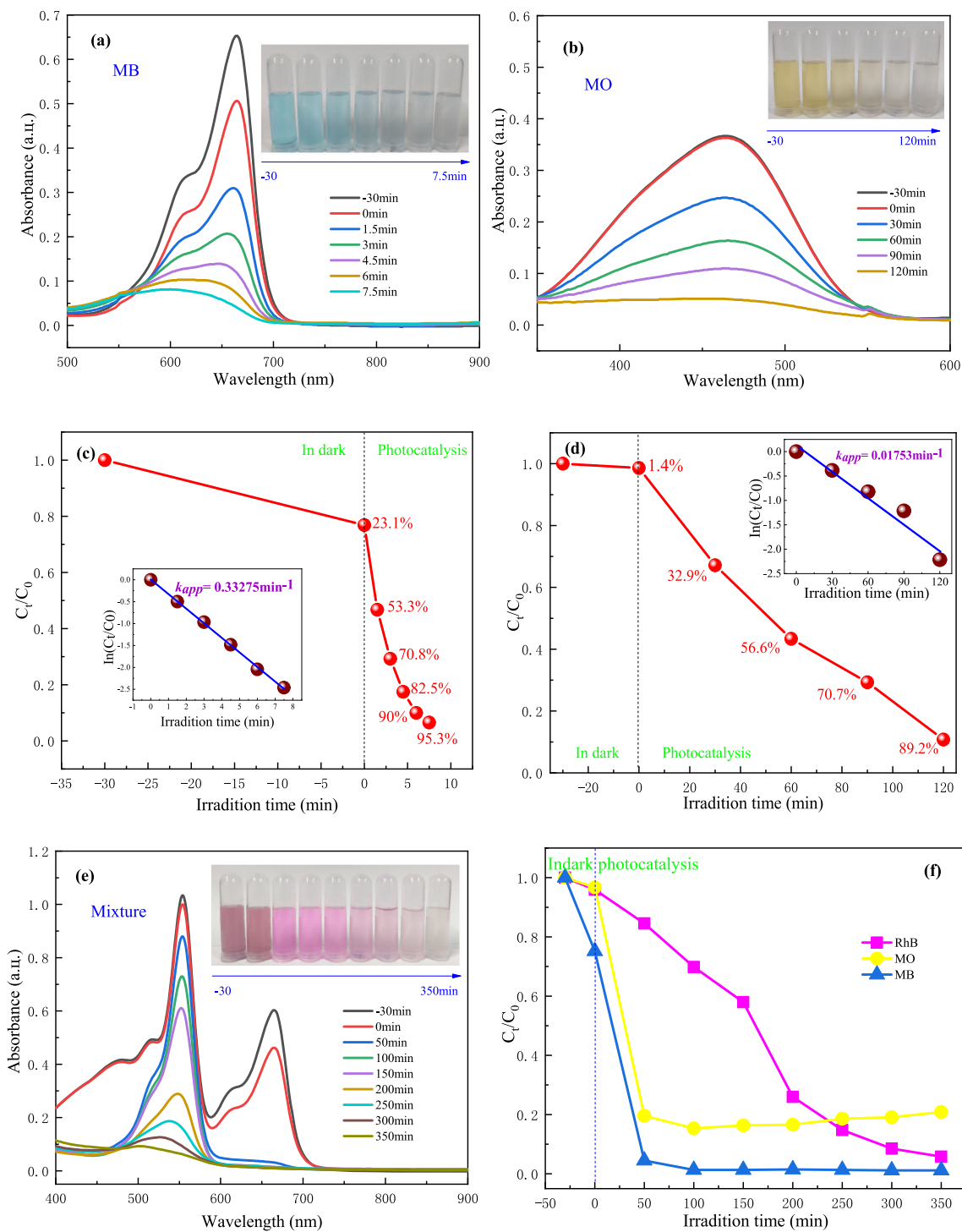
Fig. 11 **a**, **b** and UV–Vis absorption spectra of MB, MO and RhB/MO/MB mixture solutions, respectively; (**c**) and (**d**) Photodegradation curves and corresponding pseudo-one kinetic curve of MB and MO, respectively; (**f**) Photodegradation curves of RhB, MO and MB in the mixture solution

characterized by the absorption peaks at 360 and 310 nm, respectively [47–49]. By comparing the relative intensities of the absorption peaks of TC and TBBPA, their photodegradation curves versus time

were obtained, as given in Fig. 12c and d. The corresponding pseudo first-order kinetic curves of the degradation of TC and TBBPA are inserted in in Fig. 12c and d, respectively. It can be clearly seen that
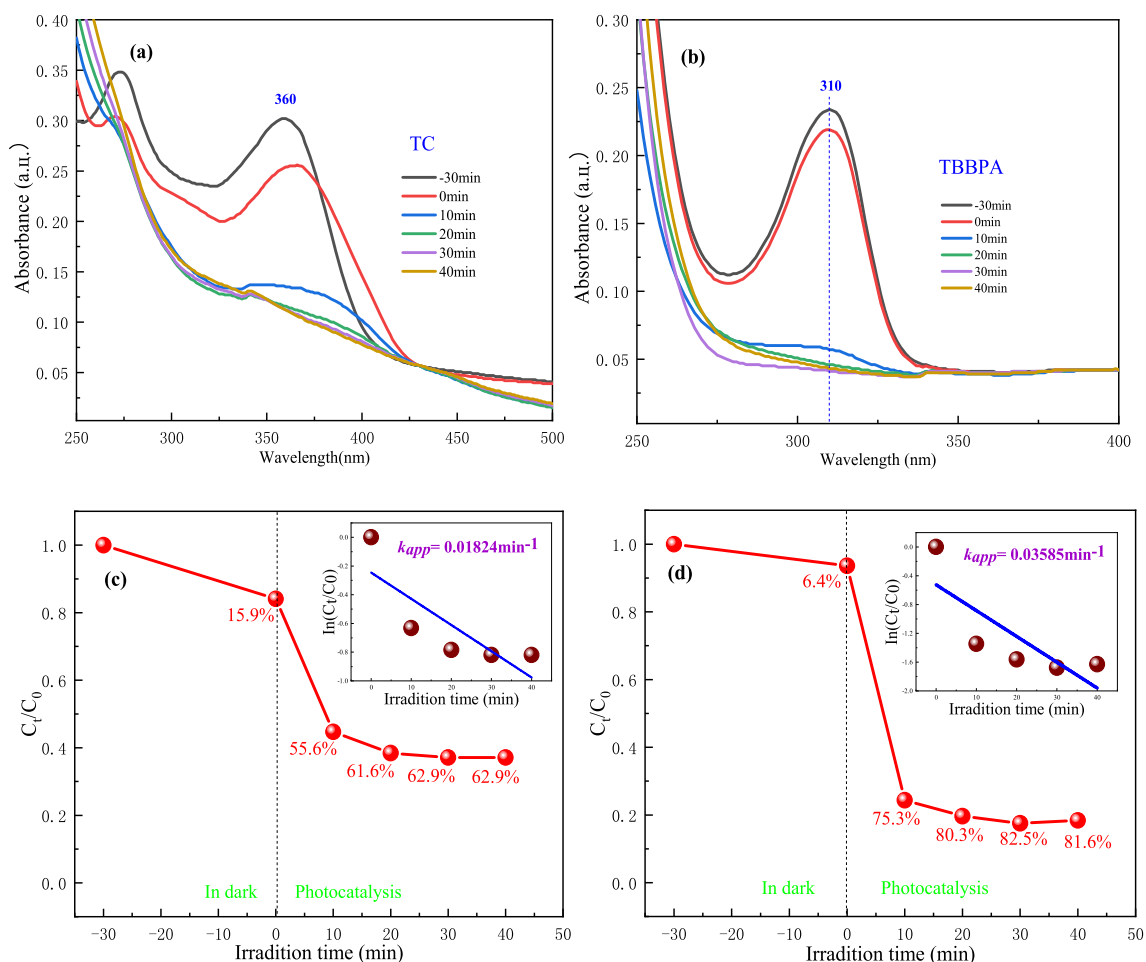
Fig. 12 **a** and **b** Ultraviolet–visible absorption spectra of TC and TBBPA photodegraded by 30 wt% AMO/BWO, respectively; **c** and **d** Photodegradation curves and the corresponding pseudo-one kinetic curves of TC and TBBPA degradation, respectively

under the action of 30 wt% AMO/BWO composite photocatalyst, TC and TBBPA are obviously degraded. When the photocatalysis progresses to 30 min, the degradation rate reach 82.5% for TBBPA (k_{app}= 0.03585 min^{-1}). For the degradation of TC aqueous solution, under 30 min of irradiation, its degradation efficiency also reaches a relatively satisfactory value 62.9% (k_{app}=0.01824 min^{-1}). The above photocatalytic degradation experiments show that the 30 wt% AMO/BWO composite photocatalyst has an industrial application prospect in removing various environmental pollutants.

Reactive species play a decisive role in the photocatalytic degradation process. In a typical photocatalytic degradation process, free radical capture experiments has conducted. The scavengers ethylenediaminetetraacetic acid (EDTA), benzoquinone (BQ) and isopropanol (IPA) were added to the photoreaction system (C_{RhB}=5 mg L^{-1},

$C_{photocatalyst}$=3 mg L^{-1}) to examine h$^+$, superoxide (•O$_2^-$) and hydroxyl (•OH), respectively. The concentration of all scavengers is 1 mmol L^{-1}. In the experiment of capturing active species of •O$_2^-$ radicals, the color of the reaction system changes abnormally under simulated sunlight. The reason for this phenomenon may be due to the light-induced reaction between BQ and RhB, which is proved by adding BQ in the RhB solution without photocatalyst, as shown in Fig. 13e. It is seen that the maximum absorption peak of RhB (554 nm) can still be used for the determination of the concentration of RhB, because it is not significantly affected by the light-induced reaction between BQ and RhB. Figure 13f shows the degradation curves of RhB without and with adding the three scavengers, which are derived from the UV–Vis absorption spectra shown in Fig. 13a–d. Obviously, the scavengers IPA and EDTA have a significant inhibitory effect on the degradation
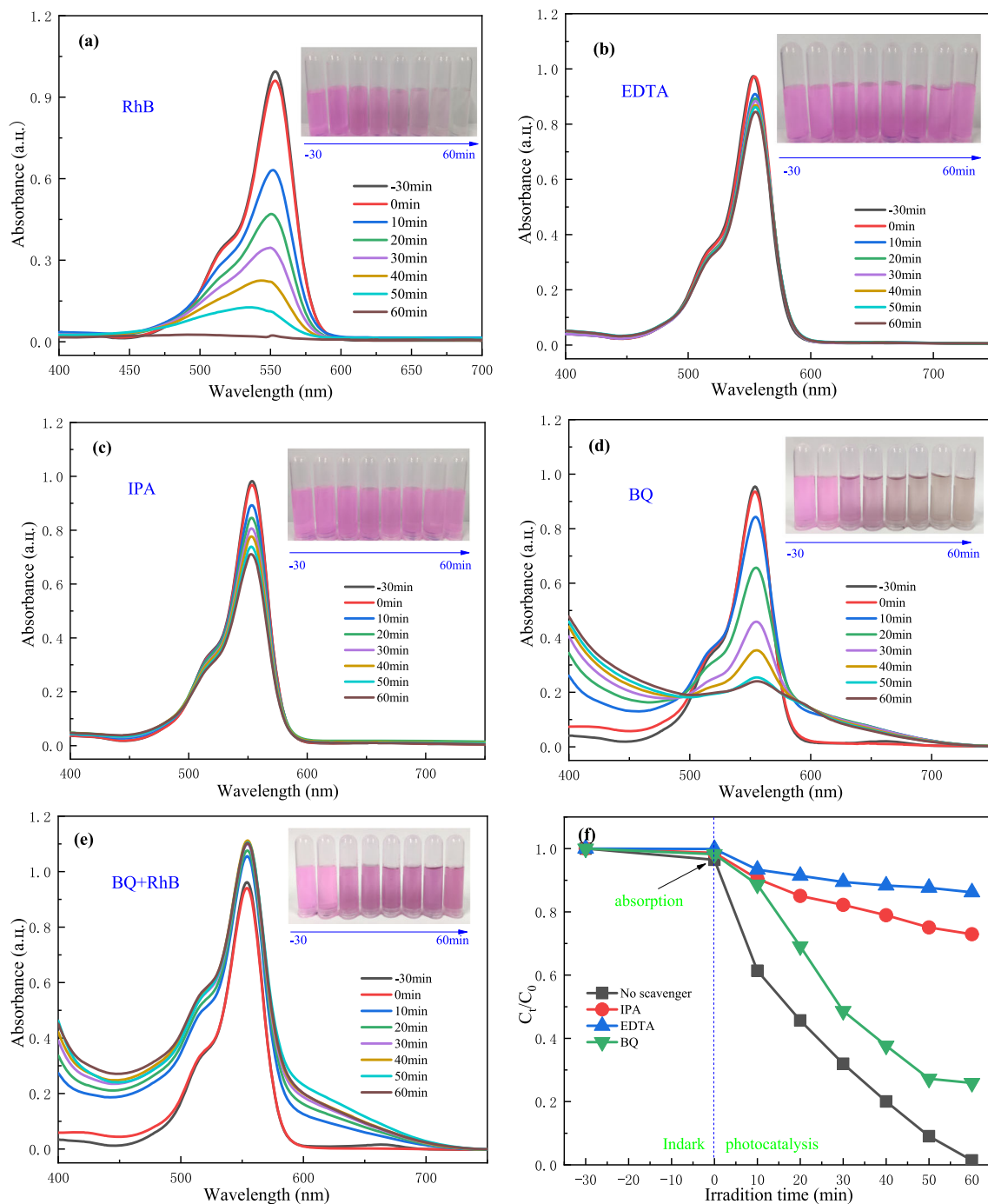
Fig. 13 The photodegradation reaction species capturing experiment: **a–d** UV–Vis absorption spectra of RhB without adding any scavenger, and with adding EDTA, IPA and BQ, respectively; **e** UV–Vis absorption spectrum of the blank RhB + BQ solution without photocatalyst; **f** the photocatalytic degradation curves of RhB without and with adding the three scavengers

of RhB, indicating that the degradation of RhB is closely related to the •OH and h$^+$ active species, while •O$_2^-$ radicals play a secondary role.

According to the Mott-Schottky diagrams measured in Fig. 14a (BWO) and b (AMO), the Mott-Schottky method [50, 51] can be used to estimate their CB potentials, which are derived to be − 0.47 and + 0.4 eV vs standard calomel electrode (SCE), respectively. Based on the relationship between SCE and normal hydrogen electrode (NHE): $V_{NHE} = V_{SCE} +$
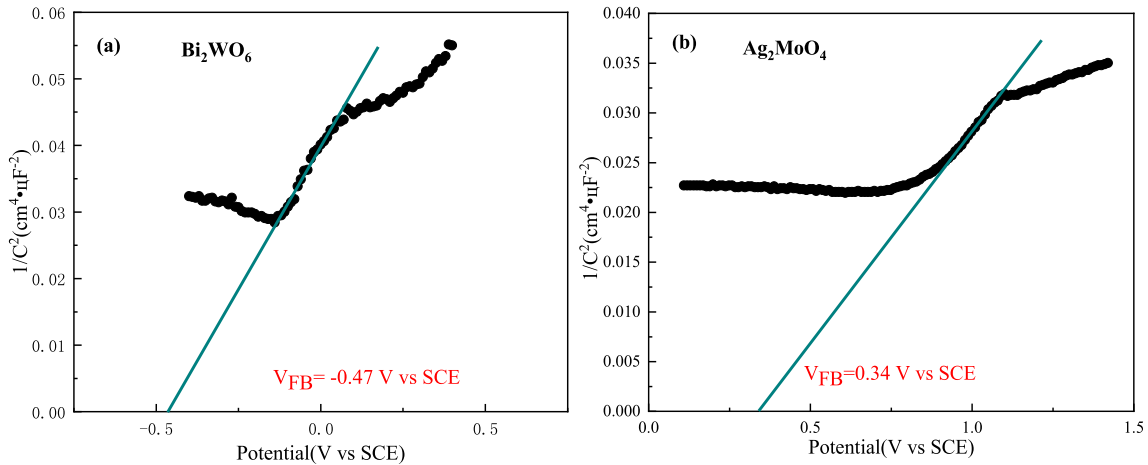
Fig. 14 Mott-Schottky diagrams of **a** BWO and **b** AMO measured at 5000 Hz

$0.059 \times pH$ (=7)+0.242 [51], and considered the bandgap of AMO (3.41 eV) and BWO (2.96 eV), the CB/VB potentials are estimated to be +1.05/+4.46 V *vs* NHE for AMO and +0.19/+3.15 V *vs* NHE for BWO. Analysis of the Mott-Schottky curves also shows that both BWO and AMO behave as n-type semiconductors.

The AMO particles are self-assembled to the hierarchical structure of rosette-like BWO, and the band structures of AMO and BWO are interlaced with each other to form the Z-scheme AMO/BWO heterojunctions, as shown in Fig. 15. Since the Fermi level of the n-type semiconductor BWO is lower than that of the n-type semiconductor AMO, electrons will spontaneously diffuse from AMO to BWO; at the same time, this electron diffusion process will generate a built-in electric field at the interface between AMO and BWO. The direction of the built-in electric field is from BWO to AMO. The built-in electric field formed will prevent the continuous diffusion of electrons, finally reaching a thermal equilibrium state at the AMO/BWO heterojunctions. However, during the photocatalytic degradation process, the thermal equilibrium state at AMO/BWO will be broken. This is due to the continuous generation of non-equilibrium holes and electrons on BWO and AMO, as shown in Fig. 15b. The built-in electric field established at the AMO/BWO heterojunction will drive the unbalanced electrons generated in the CB of the AMO semiconductor to move to the VB of the BWO semiconductor, and finally recombine with the unbalanced holes generated in the VB of the BWO semiconductor. This electron transfer method and path greatly improves the photodegradation efficiency of the catalyst, due to the prolonged lifetime of the photogenerated electrons in the CB of AMO and holes in the VB of BWO. This enables the photogenerated holes and electrons to participate in the photodegradation reaction more effectively, which is the main mechanism for the enhanced photocatalytic performance of the AMO/BWO composites. However, it is worth noting that in the analysis of XPS and TEM, metallic silver particles exist in the AMO/BWO composite materials which act as a bridge for electron transfer between BWO and AMO and promote the movement of electrons from AMO to BWO, as shown in Fig. 15c. The sufficiently positive VB potential of BWO (+3.15 V vs NHE) means that the photogenerated VB holes in BWO can React with H_2O or OH^- to generate $\bullet OH$ ($H_2O/\bullet OH$) = +2.38 V vs NEH, $E^0(OH^-/\bullet OH)$ = +1.99 V vs NHE) [52]. Moreover, according to the active species capture experiment, $\bullet OH$ radicals play an critical role in the degradation process. In addition, $\bullet OH$ radicals are not completely derived from hole reactions, the potential of sufficiently positive photo-generated holes in the VB of AMO (+4.46 V vs NHE) indicates that $\bullet OH$ radicals may be generated through their coupling with OH^- or H_2O species [53]. Holes have also been identified as an important active species in the photocatalysis. The generation of $\bullet O_2^-$ may come from the combination of the adsorbed O_2 with the light-excited electrons in higher exciting states of BWO. However, it is worth noting that the photogenerated electrons in the CB of BWO cannot react with O_2 to generate $\bullet O_2^-$, because the CB potential of BWO (+0.19 eV vs NHE) is not negative with reference to $O_2/\bullet O_2^-$ (-0.13 eV vs NHE) [54].
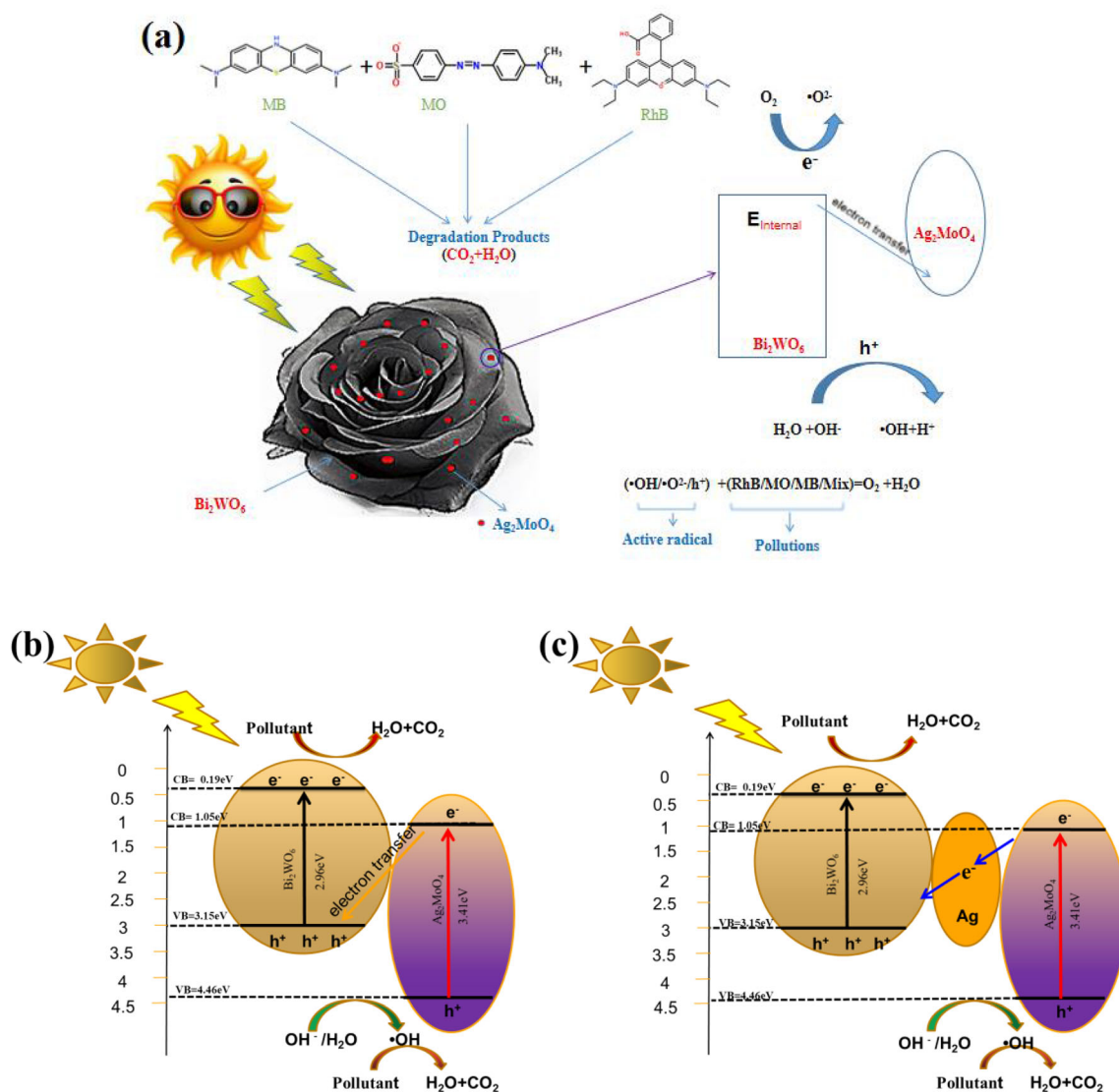
Fig. 15 **a** Z-scheme heterojunctions constructed by decorating AMO particles on a rosette-like BWO hierarchical structure; **b** and **c** Z-scheme electron transfer process of AMO/BWO and AMO/Ag/BWO, respectively

4 Conclusions

In this work, AMO nanoparticles were self-assembled on the surface of rosette-like BWO by a co-precipitation method to prepare a new type of AMO/BWO composite photocatalysts with Z-scheme heterojunctions, which have excellent photocatalytic performance. The AMO/BWO composite photocatalysts were used to photocatalytically degrade a variety of dyes and organic pollutants. The experimental results show that the 30 wt% AMO@BWO composite sample has a photocatalytic degradation rate of 98.6% for RhB. The 30 wt% AMO/BWO has the best photoexcited hole/electron pair separation and transfer efficiency, and the highest photocatalytic activity, which is 3.35 and 2.49 times higher than that of bared AMO and BWO, respectively. Based on the cross-band structure between AMO and BWO, a Z-scheme electron transfer mechanism is proposed to explain the effective carrier separation and the improvement of photocatalytic performance of the AMO/BWO heterojunction photocatalysts.

References

1. M.A. Brown, S.C. De Vito, Crit. Rev. Env. Sci. Tec. **23**, 249 (1993)

2. J. Yang, H. Zhu, Y. Peng, P. Li, J. Zhang, Nanomaterials **10**, 756 (2020)

3. M. Sboui, S. Bouattour, M. Gruttadauria, G. Marcì, S. Boufi, Nanomaterials **10**, 470 (2020)

4. P. Sharma, A.K. Singh, V.K. Shahi, A.C.S. Sustain, Chem. Eng. **7**, 1427 (2018)

5. Y. Yang, Z. Zeng, C. Zhang, D. Huang, G. Zeng, R. Xiao, C. Lai, C. Zhou, H. Guo, W. Xue, M. Cheng, W. Wang, J. Wang, Chem. Eng. **349**, 808 (2018)

6. A. Raheem, P. Prinsen, A.K. Vuppaladadiyam, M. Zhao, R. Luque, J. Clean. Prod. **181**, 42 (2018)

7. S. Silvestri, J.F. De Oliveira, E.L. Foletto, Mater. Res. Bull. **117**, 56 (2019)

8. Q.Q. Duan, J.Y. Jia, X. Hong, Y.C. Fu, C.Y. Wang, K. Zhou, X.Q. Liu, H. Yang, Z.Y. Wang, Sol. Energy **20**, 555 (2020)

9. T.T. Li, L. Xia, H. Yang, X.Y. Wang, T. Zhang, X.X. Huang, L. Xiong, C.L. Qin, G.W. Wen, A.C.S. Appl, Mater. Interfaces **13**, 11911 (2021)

10. L. Yu, X. Zhang, G. Li, Y. Cao, Y. Shao, D. Li, Appl. Catal. B: Environ. **187**, 301 (2016)

11. C. Yu, G. Li, S. Kumar, K. Yang, R. Jin, Adv. Mater. **26**, 892 (2014)

12. H.H. Xu, J. Zhang, X.Z. Lv, T.J. Niu, Y.X. Zeng, J.Z. Duan, B.R. Hou, Biofouling **35**, 719 (2019)

13. X.T. Liu, W.J. Li, H.D. Li, C.J. Ren, X.Y. Li, Y.J. Zhao, Appl. Catal. A-Gen. **568**, 54 (2018)

14. J. Zheng, F. Chang, M. Jiao, Q. Xu, B. Deng, X. Hu, Colloid Interf. Sci. **510**, 20 (2018)

15. W. Zhao, Y. Liu, Z. Wei, S. Yang, H. He, C. Sun, Appl. Catal. B: Environ. **185**, 242 (2016)

16. N. Liu, V. Häublein, X. Zhou, U. Venkatesan, M. Hartmann, M. Mačković, P. Schmuki, Nano Lett. **15**, 6815 (2015)

17. M. Diak, E. Grabowska, A. Zaleska, Appl. Surf. Sci. **347**, 275 (2015)

18. J. Jin, Q. Liang, Y. Song, S. Xu, Z. Li, C. Yao, J. Alloys Compd. **726**, 221 (2017)

19. Z. Li, X. Chen, Z.-L. Xue, Sci. China Chem. **56**, 443 (2013)

20. Y. Chen, X. Xie, Y. Si, P. Wang, Q. Yan, Appl. Surf. Sci. **498**, 143860 (2019)

21. A. Phuruangrat, P. Dumrongrojthanath, T. Thongtem, S. Thongtem, J. Ceram. Soc. Japan **125**, 500 (2017)

22. J. Zhang, L. Huang, H. Jin, Y. Sun, X. Ma, E. Zhang, H. Wang, Z. Kong, J. Xi, Z. Ji, Mater. Res. Bull. **85**, 140 (2017)

23. S.J. Li, S.W. Hu, W. Jiang, Y. Liu, J.S. Liu, J. Colloid Interface Sci. **501**, 156 (2017)

24. J. Wang, T. Lin, G.M. Zeng, Appl. Catal. B Environ. Int. J. Devot. Catal. Sci. Appl. **209**, 285 (2017)

25. J. Chen, C. Hu, Z. Deng, X. Gong, Y. Su, Q. Yang, J. Zhong, J. Li, R. Duan, Chem. Phys. Lett. **716**, 134 (2018)

26. T.R. Bastami, A. Ahmadpour, F.A. Hekmatikar, J. Indus. Eng. Chem. **51**, 244 (2017)

27. X. Zhao, H. Yang, Z. Cui, R. Li, W. Feng, Mater. Technol. **32**, 870 (2017)

28. A. Abulizi, K. Kadeer, L. Zhou, Y. Tursun, T. Dilinuer, J. Taiwan Inst. Chem. Eng. **88**, 243 (2018)

29. S.T. Guan, R.S. Li, X.F. Sun, T. Xian, H. Yang, Mater. Technol. https://doi.org/https://doi.org/10.1080/10667857.2020.1782062.

30. M. Ghobadifard, S. Mohebbi, P.V. Radovanovic, New J. Chem. **44**, 2858 (2020)

31. Y.P. Wang, X.F. Sun, T. Xian, G.R. Liu, H. Yang. Optic. Mater. **133**. https://doi.org/https://doi.org/10.1016/j.optmat.2021.110853

32. S.Y. Dong, X.H. Ding, T. Guo, X.P. Yue, X. Han, J.H. Sun, Chem. Eng. J. **316**, 778 (2017)

33. T.T. Cheng, X.F. Sun, T. Xian, Z. Yi, R.S. Li, X.X. Wang, H. Yang, Opt. Mater. **112**, 110781 (2021)

34. Y.P. Wang, R.S. Li, X.F. Sun, T. Xian, Z. Yi, H. Yang, J. Electron. Mater. https://doi.org/https://doi.org/10.1007/s11664-021-08787-x.

35. M. Golkari, H. Shokrollahi, H. Yang, Ceram. Int. **46**, 8553 (2020)

36. F. Vosoughi, A. Habibi-Yangjeh, S. Asadzadeh-Khaneghah, S. Ghosh, T. Maiyalagan, J. Photochem. Photobio. A **403**, 112871 (2020)

37. Y.P. Wang, H. Yang, X.F. Sun, H.M. Zhang, T. Xian, Mater. Res. Bull. **124**, 110754 (2020)

38. W. Shi, F. Guo, S. Yuan, Appl. Catal. B **209**, 720 (2017)

39. S.J. Sun, L. Xia, T. Zhang, H. Yang, C.L. Qin, B. Zhong, L. Xiong, X. Wu, G.W. Wen, J. Am. Ceram. Soc. https://doi.org/https://doi.org/10.1111/jace.17757

40. Y.P. Wang, X.F. Sun, T. Xian, G.R. Liu, H. Yang, Opt. Mater. **113**, 110853 (2021)

41. K. Das, D. Majhi, Y.P. Bhoi, B.G. Mishra, Chem. Eng. J. **362**, 588 (2019)

42. C.Y. Xu, Y.Y. Chen, X. Xie, K. Yan, Y.S. Si, M.H. Zhang, Q.S. Yan, J. Mater. Sci.-Mater. Electron. **31**, 8151 (2020)

43. T.Y. Wang, S.X. Liu, W. Mao, Y.C. Bai, K. Chiang, K. Shah, J. Paz-Ferreiro, J. Hazard. Mater. **389**, 121827 (2020)

44. H.J. Gao, X.X. Zhao, H.M. Zhang, J.F. Chen, S.F. Wang, H. Yang, J. Electron. Mater. **49**, 5248 (2020)

45. T. Xian, X. Sun, L. Di, H. Li, H. Yang, Opt. Mater. **111**, 110614 (2021)

46. S. Guan, H. Yang, X. Sun, T. Xian, Opt. Mater. **100**, 109644 (2020)

47. Q. Qin, Y. Guo, D. Zhou, Y. Yang, Y. Guo, Appl. Surf. Sci. **390**, 765 (2016)

48. E.O. Oseghe, A.E. Ofomaja, Photochem. Photobiolo. A **360**, 242 (2018)

49. N. Yusoff, S.A. Ong, L.N. Ho, Y.S. Wong, W. Khalik, Desalin. Water Treat. **54**, 1621 (2015)

50. F. Cardon, W.P. Gomes, J. Phys. D-Appl. Phys. **11**, L63 (1978)

51. S.Y. Wang, H. Yang, Z. Yi, X.X. Wang, J. Environ. Manage. **248**, 109341 (2019)

52. T.T. Cheng, H.J. Gao, X.F. Sun, T. Xian, S.F. Wang, Z. Yi, G. R. Liu, X.X. Wang, H. Yang, Adv. Powder Technol. **32**, 951 (2021)

53. H.J. Gao, F. Wang, S.F. Wang, X.X. Wang, Z. Yi, H. Yang, Mater. Res. Bull. **115**, 140 (2019)

54. X.F. Sun, L.J. Di, T. Xian, Y.J. Zhou, H.Q. Li, Y.S. Gao, H. Yang, J. Mater. Sci.-Mater. Electron. **32**, 623 (2021)